

Impact of helium ion irradiation on the thermal properties of superconducting nanowire single-photon detectors

Yi-Yu Hong^{1,2,3}, Yu-Ze Wang^{1,2,3}, Wei-Jun Zhang^{1,2,3*}, Jia-Hao Hu^{1,2,3}, Jia-Min Xiong^{1,2,3}, Dong-Wei Chu^{1,2,3}, Xin Ou^{1,2,3}, Wen-Tao Wu^{1,2,3}, Xiao-Fu Zhang^{1,2,3}, Hui-Qin Yu^{1,2,3}, Pu-Sheng Yuan^{1,2,3}, Hao Li^{1,2,3}, Ling Wu^{1,2,3}, Zhen Wang^{1,2,3}, and Li-Xing You^{1,2,3}

¹Shanghai Key Laboratory of Superconductor Integrated Circuit Technologies, 865 Changning Road, Shanghai 200050, China.

²National Key Laboratory of Materials for Integrated Circuits, Shanghai Institute of Microsystem and Information Technology, Chinese Academy of Sciences, 865 Changning Road, Shanghai 200050, China.

³Center of Materials Science and Optoelectronics Engineering, University of Chinese Academy of Sciences, Beijing 100049, China.

*E-mail: zhangweijun@mail.sim.ac.cn

Abstract: Superconducting nanowire single-photon detectors (SNSPDs) are indispensable for applications ranging from quantum information processing to deep-space optical communications, owing to their high detection efficiency, low dark counts, and excellent timing resolution. However, further improving the intrinsic detection efficiency (IDE) remains crucial for optimizing SNSPD performance. Ion irradiation has recently emerged as a powerful post-fabrication method to enhance SNSPD characteristics.

Here, we studied the effects of helium ion irradiation on the thermal properties of NbN SNSPDs. We systematically examine the evolution of thermal boundary conductance as a function of ion fluence ($0\text{--}1.1 \times 10^{17}$ ions/cm²), observing a 57% decrease from 127 W/m²K⁴ to 54 W/m²K⁴ with increasing fluence, followed by saturation at approximately 9×10^{16} ions/cm². At this fluence, the minimum hotspot relaxation time measurements indicate a 41% increase, rising from 17 ps to 24 ps, while the electron-phonon interaction time extends by 14%, from 11.2 ps to 12.8 ps at 10 K. Transmission electron microscopy (TEM) reveals defect formation at the NbN/SiO₂ interface (6–8 nm) and He-bubble formation within the SiO₂ layer (30–260 nm), contributing to the extended thermal relaxation time. These irradiation-induced modifications play a key role in enhancing the IDE of the treated devices.

We further demonstrate a post-irradiation SNSPD showing a saturated IDE plateau at 2000 nm from 2.7 K to 28 mK, enabled by thermal modifications and a weakly wavelength-dependent avalanche-assisted mechanism. Our findings highlight ion irradiation as a valuable tool for thermal tailoring in SNSPDs and advance the understanding of detection physics and defect engineering in superconducting optoelectronics.

Keywords: Superconducting nanowire single-photon detectors (SNSPDs), ion irradiation, thermal properties, internal detection efficiency (IDE), defect engineering

1. Introduction

Superconducting nanowire single-photon detectors (SNSPDs) are crucial for quantum optics, quantum information processing, and deep-space laser communications, owing to their high detection efficiency, low dark count rate, and minimal timing jitter [1-4]. Compared to traditional single-photon avalanche diodes (SPADs), SNSPDs exhibit superior performance in the near- and mid-infrared (MIR) spectral ranges, making them a promising technology for on-chip integration of quantum systems [5], biomedical imaging [6], and dark matter detection [7].

SNSPDs typically consist of ultrathin superconducting films (5–12 nm) made from NbN or NbTiN, which are patterned into nanowires with widths ranging from 50 to 100 nm. These detectors operate at cryogenic temperatures (2–4 K) using commercial cryocoolers. To meet emerging application demands, SNSPD research is advancing towards longer wavelength detection (e.g., MIR [8]), wider strips (e.g., microstrip detectors [9-11]), higher operating temperatures (e.g., using high-temperature superconductors [12-14]), and large-scale array integration [15,16]. Enhancing intrinsic detection efficiency (IDE) is a prerequisite for achieving high-performance SNSPDs in these new research directions.

The IDE is governed by multiple factors [17,18], including the nanowire material's energy gap, cross-sectional dimensions, photon excitation energy, and operating temperature. The bias current dependence of IDE typically exhibits a sigmoidal response with characteristic broadening [19,20]. The underlying mechanisms remain actively debated, with proposed explanations encompassing [21-24]: thermal fluctuations, Fano fluctuations (statistical energy partitioning between quasiparticles and phonons), nonlinear energy-current conversion, and nanowire nonuniformities (geometric variations or position-dependent absorption effects).

Given these fundamental dependencies, previous research has explored various fabrication-based approaches to improve SNSPD performance. For instance, optimizing film composition with amorphous materials like WSi [8,25], or Polycrystalline NbN [26] and NbTiN [12,27] has yielded promising results. Taylor et al. [8] achieved near-unity IDE at wavelengths up to 29 μm using high-resistivity WSi films, though operation at 250 mK and a low switching current (I_{sw} , $<1 \mu\text{A}$) limit practical use. Beyond fabrication-based improvements, post-processing techniques have gained attention, particularly ion irradiation [28]. In 2019, Zhang et al. [29] demonstrated that light-ion (e.g., helium, He) irradiation can introduce controlled defects using an ion implanter, modifying electrical properties such as resistivity, carrier mobility, and superconducting characteristics, ultimately enhancing IDE and detector yield [30]. Later, Xu et al. [10] used ion irradiation to boost the IDE of the NbN microstrip detectors, achieving 92.2%

system detection efficiency (SDE) at 1550 nm. In 2023, Strohauer et al. [31] employed He-ion microscopy for localized irradiation, developing a physical model to describe defect formation and sputtering effects. In 2024, Kohopaa et al. [32] demonstrated that argon/gallium ion irradiation increases disorder in superconducting films and improves the mixing of the Mo-Si materials, with TEM revealing amorphous structures and defects.

Recent studies have extended ion irradiation techniques to high-temperature SNSPDs [13,14,33]. Since 2023, Charaev et al. have fabricated SNSPDs using BSCCO-LSCO, LSCO-LCO bilayers [13], and MgB₂ [14], achieving single-photon detection above 20 K. Irradiation-induced hysteresis I-V characteristics are key for single-photon sensitivity. Yet, the precise impact of irradiation on defect formation and its influence on thermal properties remain unclear. Moreover, irradiation effects vary by materials—Batson et al. [33] found NbN SNSPDs showed no saturation up to 2.6×10^{17} ions/cm², while MgB₂ was significantly modified at 1×10^{16} ions/cm². Optimizing fluence is necessary for reproducibility and scalability.

Beyond electrical modifications, ion irradiation's impact on SNSPD thermal properties remains underexplored but is critical for performance optimization [34-39]. The SNSPD detection process involves localized energy deposition from an absorbed photon, creating a resistive normal-state region (hotspot) by breaking Cooper pairs [17]. This leads to hotspot expansion, generating a voltage pulse. Subsequently, Joule heating dissipates energy into the substrate, allowing the nanowire to return to its superconducting state for the next detection event. The photon energy relaxation process [40] is governed by the electron-electron scattering time (τ_{e-e}) and the electron-phonon interaction time (τ_{e-ph}), while the energy dissipation to the substrate depends on the phonon escape time (τ_{esc}), which is related to the thermal boundary conductance (TBC). Lower TBC improves detection efficiency by reducing phonon escape, whereas higher TBC facilitates faster reset times, enhancing high-speed detection capabilities.

Substrate selection significantly affects heat transport by determining phonon mismatch and altering TBC. For instance, SiO₂ and Al₂O₃ substrates exhibit different TBC values [37] and hotspot relaxation times (τ_{hs}) [41,42]. Previously, researchers have modified thermal coupling by selecting different substrates [37,42] or suspending the nanowire on a dielectric membrane [38] to study the impact of phonon transport. However, beyond changing substrate choice, ion irradiation can introduce localized defects or disorders in superconducting films, modifying thermal conductivity and phonon scattering. This approach may enable direct comparisons of thermal properties within the same device before and after irradiation, offering a new approach to studying the SNSPD thermal dynamics.

This work investigates the impact of He-ion irradiation on the thermal properties of NbN-based SNSPDs. Measurements of TBC across varying irradiation fluences reveal a significant decrease with increasing fluence. Additionally, τ_{e-ph} and τ_{hs} increase with fluence. The

microstructural changes in irradiated NbN thin films are analyzed using TEM. Finally, the performance of an irradiated NbN-based SNSPD with a parallel nanowire structure is explored down to ultralow temperature and over a wide wavelength range. Our findings offer new insights into defect-induced material modifications for optimizing SNSPD performance. This study also advances post-fabrication thermal engineering strategies and the detection mechanism of SNSPDs, contributing to developing high-performance SNSPDs, high-temperature SNSPDs, and MIR applications.

2. Methods

I. Sample preparation and ion irradiation simulation

Polycrystalline NbN thin films (6.5 nm and 7 nm thick) were deposited on a distributed Bragg reflector (DBR) substrate using direct-current reactive magnetron sputtering in an Ar/N₂ atmosphere at room temperature [20]. The film thickness was controlled by adjusting the sputtering time. The DBR substrate, consisting of a double-layer alternating stack of SiO₂/Ta₂O₅ on a Si wafer, was designed to enhance the nanowire's light absorption efficiency.

Subsequently, meandering nanowire structures (devices) and nanowire bridges (nanobridges) were fabricated on the same wafer using electron beam lithography (EBL) and reactive ion etching. The electrode structures were defined using ultraviolet lithography and reactive ion etching. Scanning electron microscopy (SEM) confirmed that the fabricated devices and nanobridges had a wire width of approximately 93–95 nm, as shown in Figs. 1(a) and 1(b). The fabricated devices featured an 18 μm diameter with filling factors of 31% and 73%, respectively, while the nanobridges measured ~11 μm in length.

The screened devices were mounted on an 8-inch wafer and irradiated with 30-keV He-ions using a 300-mm medium current ion implanter (Nissin Co., Exceed 2300RD). The irradiation fluence ranged from 2×10^{16} to 1.1×10^{17} ions/cm², with the total fluence achieved through multiple implantations. For instance, Device A1 underwent three sequential irradiations with fluences of 2×10^{16} , 7×10^{16} , and 2×10^{16} ions/cm², respectively, resulting in a cumulative fluence of 1.1×10^{17} ions/cm². After each implantation, its physical properties were re-measured for comparative analysis. In this study, the term “fluence” denotes the total fluence accumulated by the device at the time of measurement. He-ions were chosen to minimize chemical reaction effects, and the 30-keV energy was selected to avoid ion etching. Notably, the IDE of SNSPD

increases from 82% to 99% at 1550 nm after irradiation with a fluence of 9×10^{16} ions/cm² (see Appendix A for more details).

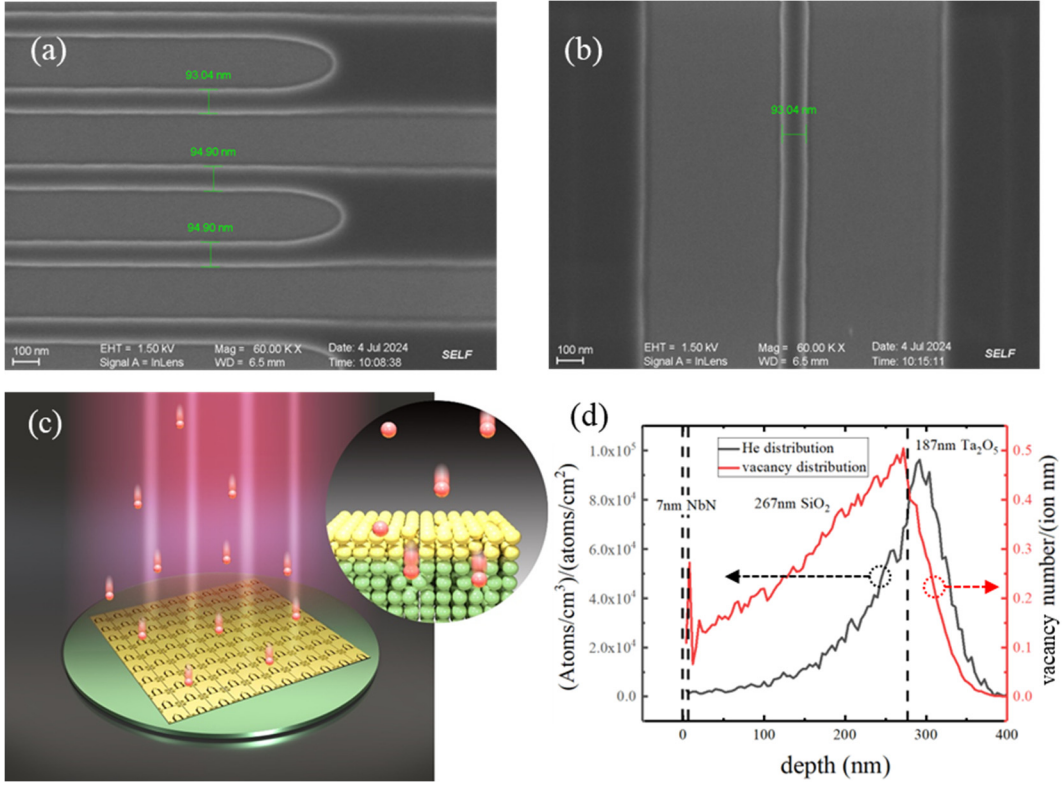


Fig. 1. SEM images of the samples: (a) meandered nanowires with circular bends; (b) a nanowire bridge; (c) Schematic illustration of an SNSPD wafer undergoing He-ion irradiation. The inset shows ions penetrating the material and generating vacancy defects; (d) Simulated depth profiles of He-ion concentration (black line) and vacancy defects (red dashed line) induced by ion irradiation.

Figure 1(c) is a schematic diagram of ion irradiation. Figure 1(d) shows the calculated distribution of He-ion concentration and vacancy defects extracted from the SRIM calculation (Appendix B). The implanted ions fully penetrated the NbN thin film and were distributed near the interface of the first SiO₂/Ta₂O₅ bilayer (i.e., depth \sim 290 nm).

II. Analysis of the thermal relaxation process in SNSPD

In SNSPDs, the absorption of a photon initiates a sequence of thermal relaxation processes that ultimately determine the detector's response time and efficiency. Figure 2 provides a schematic representation of these processes. The incident photon excites electrons in the NbN nanowire, forming a hotspot due to electron-phonon interactions. This interaction is characterized by τ_{e-ph} , which governs the rate at which electron energy is transferred to the lattice. In disordered superconductors like NbN, τ_{e-ph} is primarily determined by the density of electronic states at the Fermi level (N_0) and the phonon spectrum. As the hotspot evolves, energy

dissipation occurs through electron-phonon interactions, and phonons transfer energy to the substrate via the TBC, denoted as β .

The total thermal relaxation time (τ_{th}) characterizes the above processes, incorporating both mechanisms, known as the two-temperature model [40,43]. According to this model, Semenov et al. derived the following expression for τ_{th} in NbN thin films:

$$\tau_{th} = \tau_{e-ph} + (1 + C_e/C_{ph})\tau_{esc}, \quad (1)$$

where C_e and C_{ph} are the specific heats of electrons and phonons, respectively. The phonon escape time (τ_{esc}) is influenced by the acoustic mismatch between the NbN film and the substrate, with a lower β leading to increased τ_{esc} , thereby prolonging τ_{th} .

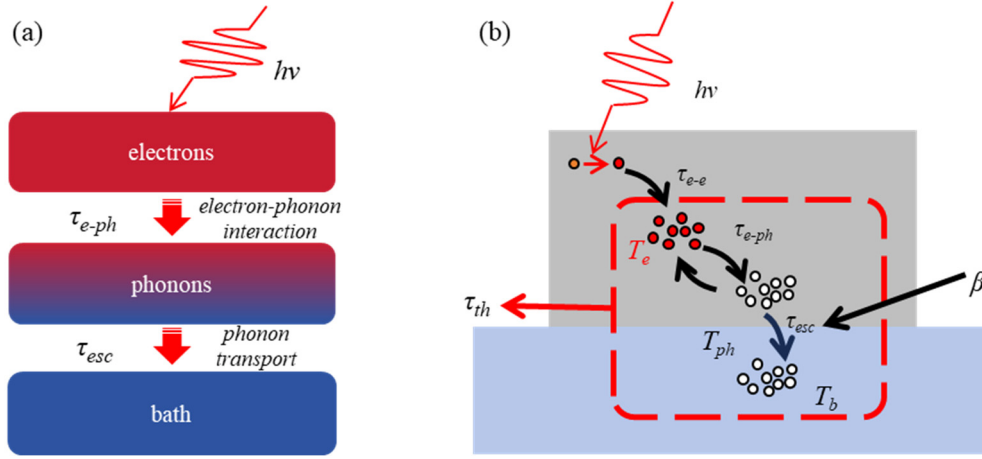


Fig. 2. Schematic of the thermal relaxation process in the nanowire after photon absorption: (a) macroscopic view of photon energy conversion across different systems [34]; (b) microscopic view highlighting key physical parameters [40], where T_e and T_{ph} represent the effective temperatures of electrons and phonons, respectively. T_b is the bath temperature. β refers to the TBC.

It is important to distinguish between τ_{th} and τ_{hs} . While τ_{th} characterizes the overall energy dissipation process in the system, τ_{hs} specifically refers to the recovery of the superconducting state within the hotspot region. τ_{hs} is affected not only by thermal relaxation but also by current redistribution and superconducting vortex dynamics. To investigate the thermal properties, in the following sections, we measured τ_{e-ph} , β , and τ_{hs} in NbN thin film and SNSPDs before and after ion irradiation, respectively.

3. Results

I. Characterization of electron-phonon scattering time before and after ion irradiation

Following established methodologies [23,35], we extracted key superconducting film

parameters (such as τ_{e-ph}) by measuring the sheet resistance (R_s) under external magnetic fields ($H = 0-9$ T) across various temperatures (8–20 K). The measurement procedure is detailed in Appendix G. The relationship between the sheet magnetoconductance (σ) and R_s is given by:

$$\sigma(H, T) = 1/R_s. \quad (2)$$

The excess magnetoconductance ($\delta\sigma$) which accounts for deviations from R_s at zero field, is expressed as:

$$\delta\sigma(T) = \frac{1}{R_s(B,T)} - \frac{1}{R_s(0,T)} \quad (3)$$

Figures 3(a) and 3(b) show the normalized excess magnetoconductance of NbN thin films before and after irradiation at a fluence of 9×10^{16} ions/cm² as a function of the cyclotron frequency $\omega_H = 4eDH/\hbar$ across different temperatures. ω_H is calculated in a disordered conductor with the reduced Planck's constant (\hbar) and the electron diffusion constant (D_e) of normal-state electrons. As ω_H increases, the magnitude of the negative excess magnetoconductance increases. The contributions to $\delta\sigma$ from weak localization, Maki-Thompson, Aslamazov-Larkin, and density of states effects are described in Ref. [23]. The experimental data fit well with the collective interplay of these four mechanisms.

The electron dephasing time (τ_ϕ), is defined as the inverse sum of rates corresponding to various phase-breaking scattering mechanisms, including electron-electron interactions (e-e), electron-phonon interactions (e-ph), and electron-environment fluctuations (e-fl). It can be expressed as [44]:

$$\tau_\phi^{-1} = \tau_{e-e}^{-1} + \tau_{e-ph}^{-1} + \tau_{e-fl}^{-1}, \quad (4)$$

where

$$\tau_{e-e}^{-1} = \frac{k_B T}{\hbar} \frac{1}{2C_1} \ln(C_1), \quad (5)$$

$$\tau_{e-ph}^{-1} = \alpha_{e-ph}^{-1} \left(\frac{T}{T_{C0}} \right)^n \quad (6)$$

$$\tau_{e-fl}^{-1} = \frac{k_B T}{\hbar} \frac{1}{2C_1} \frac{2 \ln(2)}{\ln(T/T_C) + C_2}, \quad (7)$$

with $C_1 = \frac{\hbar}{(R_S N e^2)}$ and $C_2 = 4 \ln(2) [(\ln(C_1))^2 + 128 C_1 / \pi] - \ln(C_1)$.

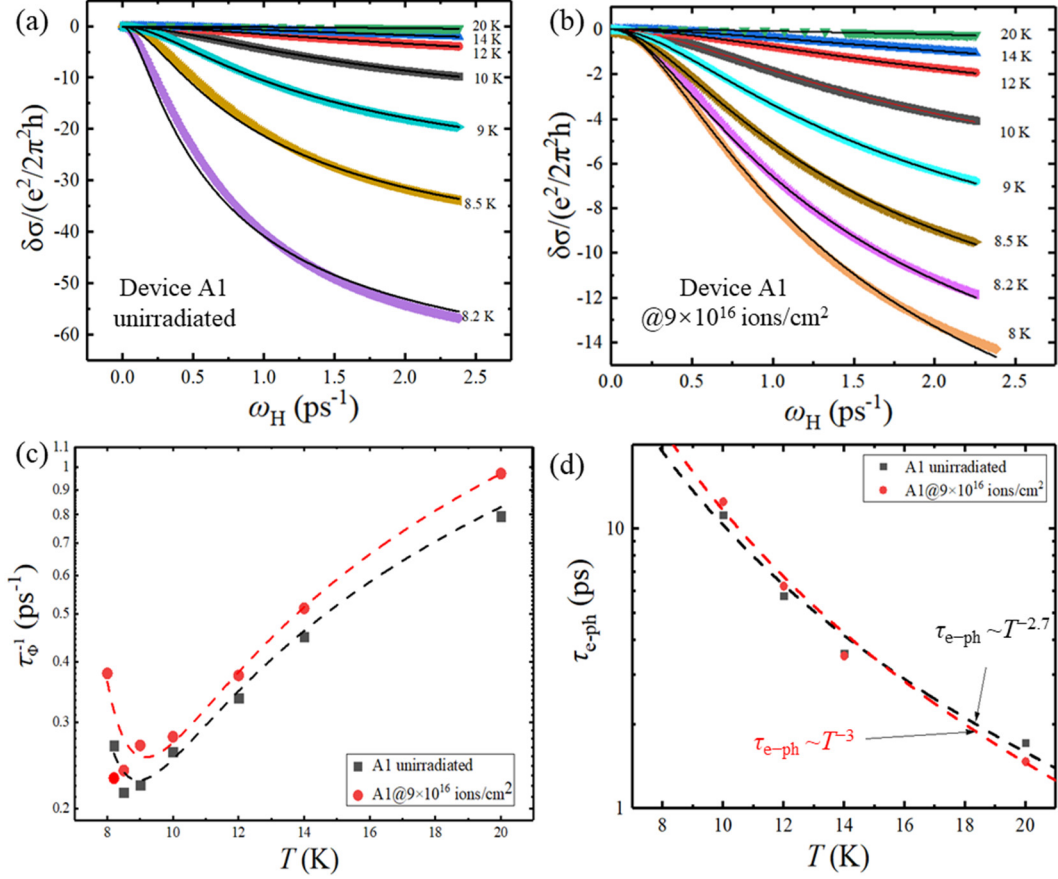


Fig. 3. Measurement data and their fits for the excess magnetoconductance of NbN films at various temperatures: (a) before irradiation; (b) after irradiation; (c) deduced τ_{ϕ}^{-1} for the devices before and after irradiation, where dashed lines are fitted using Eqs. (4) – (7); (d) deduced τ_{e-ph} for the devices before and after irradiation; dashed lines are fitted with $\tau_{e-ph} \sim T^{-n}$, where n is approximately 2.7 for unirradiated and 3.0 for irradiated samples, respectively.

After fitting the excess magnetoconductance data before and after irradiation, we extract the τ_{ϕ}^{-1} as shown in Fig. 3(c). It is observed that τ_{ϕ}^{-1} in the thin film increases ($\sim 11\%$ at 10–14 K) after irradiation, suggesting an enhancement of the electron-phonon interaction. This is likely due to irradiation-induced lattice distortion and defect formation in NbN layer, contributing to an increased scattering probability between electrons and phonons.

The τ_{e-ph} is determined using Eqs. (4–6) based on the data in Figure 3(c). Figure 3(d) presents its temperature dependence before and after irradiation. After irradiation, τ_{e-ph} increases at 10–12 K but decreases at 14–20 K. At $T = 10$ K, it rises from 11.2 ps to 12.8 ps. Additionally, τ_{e-ph} follows a power-law dependence on temperature ($\tau_{e-ph} \sim T^{-n}$) between 10–20 K, with exponents of $n \approx 2.7$ (unirradiated) and 3.0 (irradiated), aligning with previous studies on disordered NbN

films. For instance, Sidorova et al. [35] reported $n \approx 3.2\text{--}3.8$ in highly disordered NbN films, suggesting the NbN films studied here fall within a moderate disorder regime.

II. Measurement of the thermal boundary conductance before and after ion irradiation

We use electrical measurements to estimate the TBC between the nanowires and the dielectric substrate, leveraging the Skocpol-Beasley-Tinkham (SBT) model and recent advances in phonon transport analysis [37,39]. This framework assumes that phonon black-body radiation at the nanowire-substrate interface is the dominant hotspot cooling mechanism, with heat dissipation following a T^4 dependence. Consequently, when the hotspot reaches thermal equilibrium, this leads to the modified expression:

$$\beta w^2 (T_{hs}^4 - T_b^4) = I_{hs}^2 R_s (|x| < x_N), \quad (7)$$

where β and T_{hs} are fitting parameters; w and T_{hs} denote the nanowire width and the hotspot temperature, respectively. I_{hs} is the self-heating hotspot current (I_{hs}), or the hysteresis current, defined as the constant current plateau at non-zero voltages during the downward voltage sweep of the current-voltage (I-V) curve (Appendix C).

Figure 4(a) shows a magnified view of the typical I-V curve measurements for the irradiated device (A1) with a filling factor of 31% at various temperatures. I_{hs} , marked by an arrow in the figure, decreases from 1.06 μA at 2.3K to 0.79 μA at 5.3K as temperature rises, while the hysteresis plateau width gradually narrows.

Figure 4(b) presents the measured $I_{hs}(T)$ data before and after irradiation, along with the corresponding fits using Eq. (7). For devices fabricated from the same wafer, both I_{hs} and T_c exhibit some variation pre- and post-irradiation (at a fluence of 9×10^{16} ions/cm²). Specifically, I_{hs} decreases from 2.18–2.3 μA to 1.01–1.15 μA , while T_c drops from 7.88–7.95 K to 7.03–7.10 K after irradiation.

Figure 4(c) shows the transformed representation of Figure 4(b), where the slope of the linear fit corresponds to the TBC value. Notably, the un-irradiation TBC is approximately 126 to 130 W/m²K⁴, while the post-irradiation TBC ranges from 51 to 63 W/m²K⁴, indicating some degree of variation. This is possible due to the differences in thin film quality and interface bonding strength, which impact phonon transport efficiency.

Figure 4(d) summarizes statistical results from multiple samples across different irradiation fluences, revealing a clear trend: TBC decreases with increasing irradiation fluence. However, beyond a threshold fluence of approximately 9×10^{16} ions/cm², the TBC stabilizes, likely due to defect density saturation, the dominance of interface thermal conductance in heat transport, and the formation of lateral localized thermal channels (Appendix L). Moreover, before irradiation, the average TBC is 127 W/m²K⁴ ($T_c=7.95$ K), whereas, after irradiation at 9×10^{16} ions/cm², it

decreases to $54 \text{ W/m}^2\text{K}^4$ ($T_c = 7.03 \text{ K}$), marking a substantial reduction by a factor of approximately 2.4 (or a 57% decrease from the initial value).

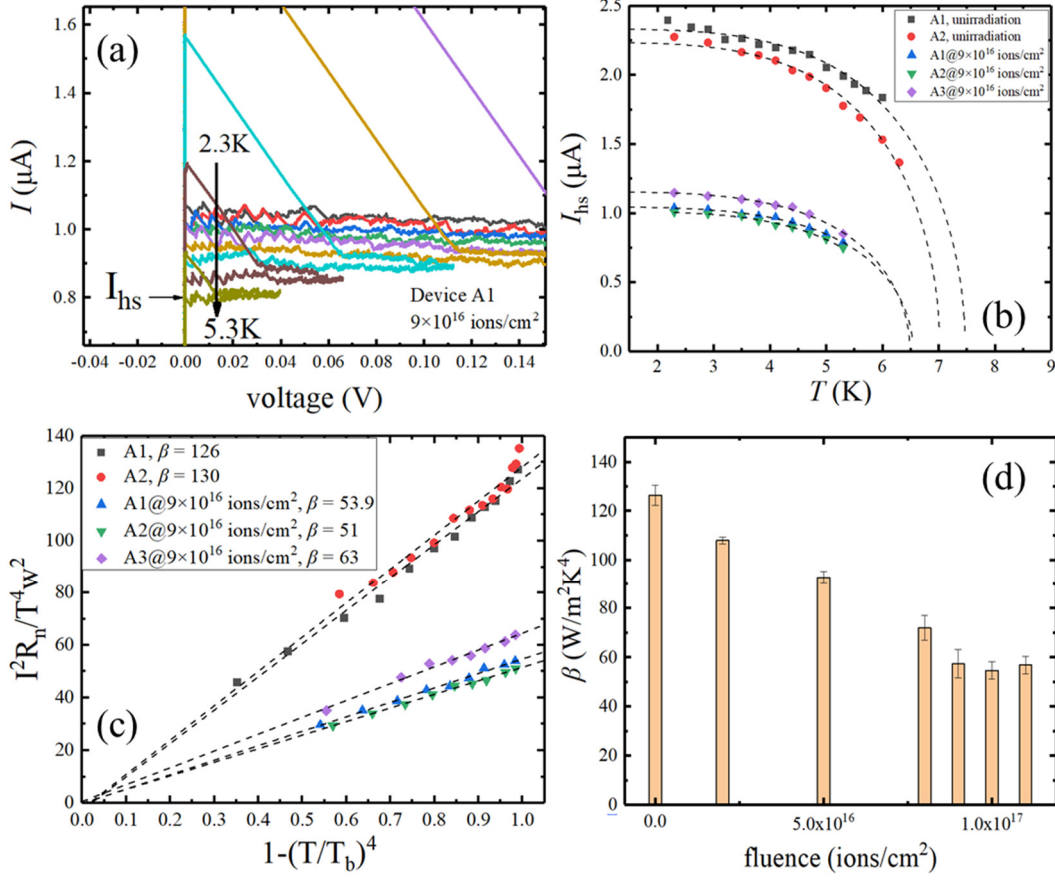


Fig. 4. (a) Magnified view of I-V characteristics of the irradiated device A1 (at $9 \times 10^{16} \text{ ions/cm}^2$) measured at different temperatures, where the hotspot current, I_{hs} at 5.3 K is indicated by an arrow. (b) Temperature dependence of I_{hs} for devices before and after irradiation. Devices A1 to A3 were irradiated, while Devices D1 to D3 represent unirradiated devices. (c) Result of the coordinate axis transformation from Fig. 2(d), where the slope of the linear fit corresponds to the TBC (i.e., β) of the tested device. (d) Variation trend of the fitted TBC for the same batch of devices under different fluences, with average values (bars) and error bars ($\pm 5\%$).

Interestingly, the TBC demonstrates a certain sensitivity to irradiation fluence, suggesting that controlled ion irradiation could serve as a viable method for tuning the TBC of SNSPDs, thereby influencing their thermal dissipation performance.

III. Investigation of the hotspot relaxation time before and after ion irradiation

We measured τ_{th} using the detection tomography method proposed by Marsili et al. [41]. At sufficiently low bias currents, detection occurs only when two photons create overlapping hotspots, enabling us to probe quasiparticle relaxation dynamics. Experimental details are

provided in Appendix D.

Figure 5(a) presents the result for device A1 (2×10^{16} ions/cm² fluence), demonstrating the identification of the two-photon detection regime by measuring the photon count rate (PCR) as a function of bias current ($0.3I_{sw}$ to $0.7I_{sw}$). A fitted slope (k) of ~ 2 in these curves confirms operation in the two-photon regime, with the bias current ratio within $0.4I_{sw}$ to $0.5I_{sw}$.

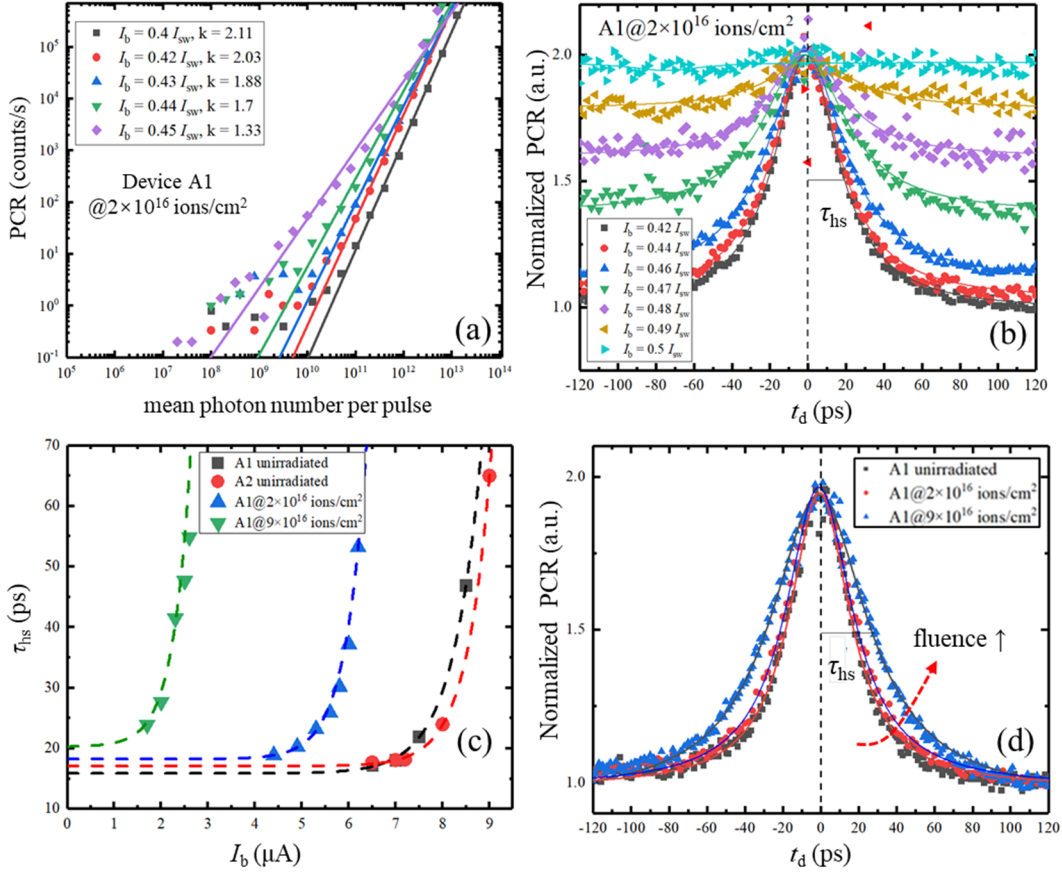


Fig. 5. (a) Photon count rate (PCR) as a function of mean photon number per pulse at different bias currents, with the fitted lines indicating the two-photon detection regime. (b) Normalized PCR as a function of delay time (t_d) after irradiation. (c) Comparison of hotspot relaxation time (τ_{hs}) before and after irradiation across various devices as a function of bias current. Dashed lines are exponential decay function fits. (d) Normalized PCR as a function of t_d for device A1 corresponding to τ_{hs-min} at each irradiation fluence. The dashed arrow indicates the fluence increases.

To extract τ_{th} , optical pulse pairs with a variable delay (t_d) were coupled into the SNSPD, and the PCR was measured as a function of t_d . The data were fitted with a Lorentz function and normalized to 2 at $t_d = 0$ ps, while optical interference effects were disregarded within $t_d \leq \pm 2$ ps. As shown in Figure 5(b), the resulting Lorentzian profiles broaden with increasing bias current, with τ_{th} defined as the full width at half maximum (FWHM) of these curves.

Figure 5(c) summarizes the dependence of τ_{hs} on bias current for multiple devices before and after irradiation. The τ_{hs} increases with bias current, consistent with the reported findings [41,42], likely due to current-induced suppression of the superconducting gap, which affects quasiparticle recombination rates. At higher currents, this increase is more pronounced, aligning with the influence of Fano fluctuations and vortex dynamics described by Kozorezov et al. [21]. Since τ_{hs} decreases with increasing current and saturates, we define $\tau_{\text{hs-min}}$ as the minimum observed value at the lowest bias current for device comparison. For unirradiated devices, $\tau_{\text{hs-min}}$ was ~ 17.3 ps at $6.5 \mu\text{A}$, with a fitted minimum of $15.9 - 16.9$ ps. After irradiation at 2×10^{16} ions/cm², $\tau_{\text{hs-min}}$ increased to 19.6 ps at $4.86 \mu\text{A}$ and 24 ps at $1.75 \mu\text{A}$. The bias current of the irradiated devices is lower than that of the unirradiated devices, leading to reduced heat generation from the hotspot. However, the measured τ_{hs} after irradiation remains significantly longer, indicating a substantial suppression of heat dissipation. Figure 5(d) shows the normalized PCR vs. t_d at $\tau_{\text{hs-min}}$ for device A1 under different irradiation fluences ($0, 2 \times 10^{16}$, and 9×10^{16} ions/cm²), revealing a fluence-dependent increase in $\tau_{\text{hs-min}}$, which becomes more pronounced at higher fluences.

IV. Analysis of microstructural changes in NbN thin films induced by irradiation

To investigate the effects of ion irradiation on the microstructure of the samples, we performed transmission electron microscopy (TEM, JEM-2100F, JEOL) analysis on the samples before and after irradiation. Figures 6(a) and 6(b) present the magnified TEM images near the NbN/SiO₂ interface and the corresponding fast Fourier transform (FFT) of each layer (inset), respectively. Before irradiation, the interface between NbN and SiO₂ is visible, with an NbN thickness of $6.5-7.4$ nm and a surface oxidation layer thickness of $0.7-2.0$ nm. After irradiation, the interface between the two layers becomes blurred, accompanied by disorder (as indicated by the FFT in the inset). Figure (d) and its corresponding FFT analysis reveal the formation of a defect layer in the SiO₂ near the NbN side, with a thickness of $5.8-8.0$ nm. These observations align well with the SRIM simulation results in the appendix B, where the vacancy defect density reaches its peak at the NbN/SiO₂ interface.

FFT analysis reveals the coexistence of polycrystalline and amorphous phases in the NbN film layer both before and after irradiation, with no distinct or well-ordered crystalline NbN

observed. The SiO₂ film layer remains amorphous throughout, while the FFT diffraction spots of the irradiated film became further blurred, indicating a higher defect density.

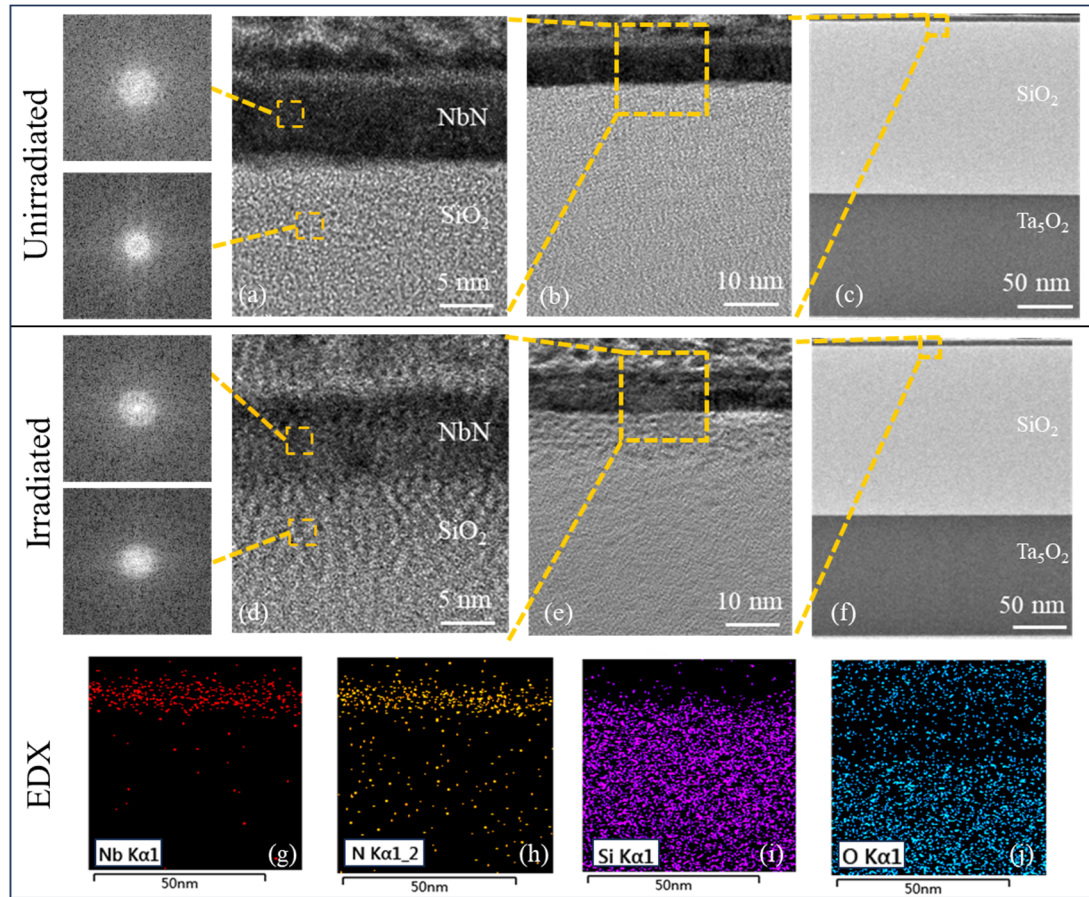


Fig. 6. TEM cross-sectional images of NbN thin films, comparing unirradiated and irradiated samples (9×10^{16} ions/cm²), taken from non-nanowire regions of the chips. (a) & (b), (c) & (d), and (e) & (f) correspond to scale bars of 5 nm, 10 nm, and 50 nm, respectively. A protective platinum layer was deposited atop the NbN film for TEM imaging. Insets of (a) and (b) are the FFT analysis for the NbN layer and SiO₂ layer, respectively. (g)–(j): EDX maps for Nb, N, Si, and O elements, respectively.

Figures 6(b), 6(c), 6(e), and 6(f) further illustrate TEM images over a greater depth scale before and after irradiation, respectively. For instance, the interface between SiO₂ and Ta₂O₅ is shown in Figure 6(f), where no significant vacancy defect layer is observed within a depth of approximately 450 nm. However, some dark contrast regions are visible, which are possibly related to He-induced bubble formation. Their density increases with irradiation fluences, and they are distributed in the range of 30–260 nm (Appendix E).

Figures 6(g)–6(j) present the energy-dispersive X-ray spectroscopy (EDX) mapping of the elemental composition in the irradiated films. The displaced Nb atoms are relatively sparse

(Figure 6(g)) due to their high atomic mass, making them less susceptible to displacement under irradiation by low-mass He ions. In contrast, a substantial number of displaced N atoms are observed (Figure 6(h)), widely distributed within the SiO₂ layer to a depth of approximately 50 nm. The Si element is primarily concentrated in the SiO₂ layer (Figure 6(i)), while the O element exhibits a broader distribution, with a higher density of displacements or vacancies appearing at a depth of 4–14 nm beneath the NbN layer (Figure 6(j)). The EDX mapping results are consistent with the SRIM simulation (Appendix B).

After completing our initial experiments, we came across a recent study on arXiv [45] that reported TEM observations of NbTiN/SiO₂/Si multilayers subjected to He ion microscope irradiation. Their findings indicated that high-fluence irradiation (2×10^{17} ions cm⁻²) induced significant amorphization at the SiO₂/Si interface, extending to a depth of 350 nm, where a distinct deep bubble layer was observed. In contrast, our TEM results reveal that the most pronounced structural modifications occur at the NbN/SiO₂ interface. Besides, we also identified dark contrast regions, likely associated with He-induced bubble formation. We attribute these differences to the lower irradiation fluence used in our study and variations in layer stacking compared to Ref. [45]. Specifically, while irradiation-induced amorphization is more pronounced in the crystalline Si substrate, it remains less distinguishable in the inherently amorphous SiO₂ layer.

4. Demonstration: enhanced mid-infrared SNSPD performance via ion irradiation

Ion irradiation improves the IDE of SNSPDs but reduces I_{sw} , impacting the timing jitter. This trade-off can be mitigated by increasing the film thickness [3] or employing parallel nanowires, such as in the SC-2SNAP structure [46-49]. Here, we demonstrate enhanced long-wavelength photon detection in parallel nanowires through irradiation-induced modifications and the implementation of an avalanche mechanism with weak wavelength dependence. This provides a promising strategy for MIR photon detection. In addition, the parallel nanowire design helps improve timing performance in amorphous superconductors like WSi and MoSi operated in MIR [8,50].

An irradiated NbN SNSPD (Device J3) with an SC-2SNAP configuration (Appendix H). The device features an $18 \times 18 \mu\text{m}^2$ active area with nominally 6.5 nm thick, 90 nm wide nanowires

arranged on a 160 nm pitch, fabricated via conventional EBL for efficient fiber coupling and high SDE. He-ion irradiation (1×10^{17} ions/cm²) reduced T_c from 7.43 K to 6.28 K and I_{SW} from 22.0 μ A to 10.2 μ A (measured at 2.1 K). More details can be found in Appendix Table III.

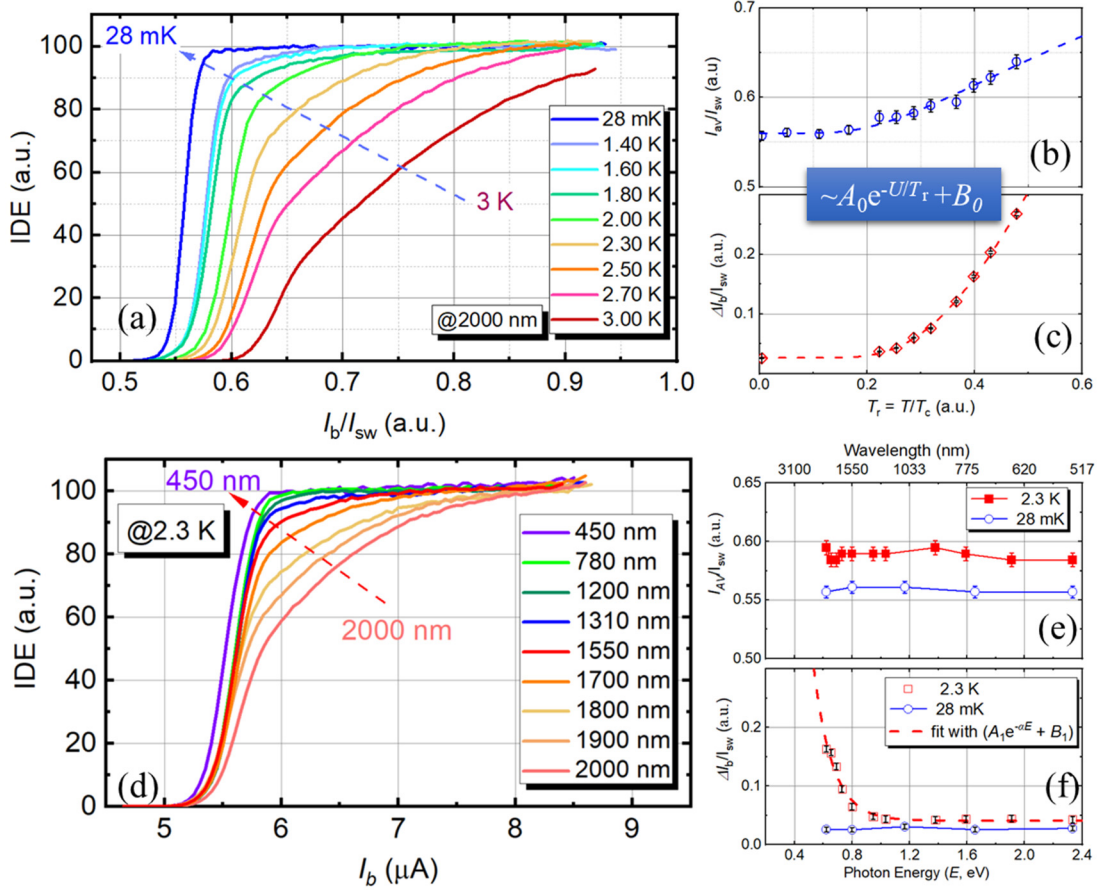


Fig. 7. Demonstration of a high-IDE NbN SNSPD for MIR detection using ion irradiation. (a) Temperature dependence of the IDE as a function of I_b/I_{sw} measured over the range of 3.0 K to 28 mK under illumination with 2000 nm wavelength photons. (b) I_{AV}/I_{SW} ratios and (c) $\Delta I/I_{SW}$ ratios as a function of reduced temperature at a wavelength of 2000 nm. (d) Wavelength dependence of the IDE as a function of I_b/I_{sw} measured at 2.3 K under illumination with wavelengths ranging from 450 to 2000 nm. (e) I_{AV}/I_{SW} ratios and (f) $\Delta I/I_{SW}$ ratios as a function of photon energy (or wavelength, top label) at two temperatures. Arrows indicate that the width of the IDE saturation plateau increases as temperature (or wavelength) decreases. The dashed lines represent fitted curves.

Figure 7(a) presents the IDE as a function of the normalized bias current under 2000 nm illumination, measured across temperatures ranging from 3.0 K to 28 mK. As the temperature decreases, a saturation plateau emerges at 2.7 K, becoming broader and steeper, demonstrating enhanced sensitivity beyond 2000 nm. For instance, at 28mK, the plateau width exceeds 5.0 μ A, and a current transition width (ΔI) is below $0.027I_{SW}$ ($\sim 0.35 \mu$ A). ΔI is defined as the

difference between the normalized currents corresponding to 90% IDE and 10% IDE.

The detection threshold current is expressed in terms of the avalanche current (I_{AV}), defined as the bias current at which the first derivative of IDE(I_b) reaches its peak [48] (Appendix I). Figure 7(b) illustrates that the avalanche current ratio, I_{AV}/I_{SW} , decreases with reduced temperature ($T_r = T/T_c$) and saturates at low temperatures—for example, dropping from 0.64 at 3 K ($T_r = 0.48$) to 0.56 at 28 mK ($T_r \approx 0$). A similar trend is observed for the normalized transition width $\Delta I/I_{SW}$, as shown in Figure 7(c).

Remarkably, all the experimental data in Figures 7(b) and 7(c) are well described by a thermal activation relation [24] ($\propto e^{-U/T_r}$, U is the effective potential barrier). This finding, previously unreported in the context of SNSPDs, suggests that IDE transition broadening may originate from strong thermal fluctuations that increase superconducting nonuniformities at high temperatures. Meanwhile, Fano fluctuations may introduce randomness, e.g., leading to a slight residual broadening of the transition at ultra-low temperatures.

Figure 7(d) shows the IDE as a function of normalized bias current under 450–2000 nm (or photon energy of 0.6–2.4 eV) illumination, measured at 2.3 K. As shown in Figure 7(e), the I_{AV}/I_{SW} ratio remains nearly constant across the measured wavelength, e.g., 0.589 ± 0.005 at 2.3 K and 0.559 ± 0.002 at 28 mK, suggesting a wavelength weak-dependent avalanche mechanism. This behavior distinguishes the SC-2SNAP configuration from standard SNSPDs [22,48,51], where I_{co} of SNSPD varies significantly with photon energy and demonstrates a nonlinear energy-current relation (e.g., increasing from 0.3 to $0.9I_{SW}$ for an 85 nm-wide nanowire [51]).

In Figure 7(f), at 2.3K, $\Delta I/I_{SW}$ rapidly increases for wavelengths beyond 1310 nm and follows an exponential dependence, $e^{-\alpha E}$, where α depends on material and geometry. In contrast, at 28 mK, $\Delta I/I_{SW}$ remains nearly constant across the measured wavelengths. Photon energy influences $\Delta I/I_{SW}$ through local excitation, with Fano fluctuations playing a greater role at lower photon energies, increasing hotspot variability, and broadening $\Delta I/I_{SW}$. As photon energy increases, the relative impact of Fano fluctuations diminishes, resulting in a more deterministic transition. The broadening ΔI was also observed in a MoSi SNSPD over a broad wavelength range (750–2050 nm) at 750 mK [22]. However, the anticipated saturation of ΔI at high photon energies was not clearly resolved in their study, which may be attributed to the limited spectral range of

the measurements. We noticed that the IDE broadening caused by temperature variations is more significant than that induced by changes in photon energy.

To assess the general applicability of the exponential fits, we also examined literature data from standard SNSPDs, which follows the same trend. Further details are available in Appendix J. The SC-2SNAP design reduces decay time to ~ 20 ns, while the system timing jitter, measured with a room-temperature amplifier, shows at 95 ps at 2.3 K and increases to 140 ps at 3.0 K (Appendix K). These findings offer interesting insights for optimizing SNSPDs for high-temperature and long-wavelength applications.

5. Discussions

We now present a comprehensive analysis of our experimental findings, reviewing the impact of He-ion irradiation on the thermal transport properties of NbN films and its implications for SNSPD performance, particularly for IDE enhancement. A summary of the key experimental results is provided in Appendix Table II.

Initially, ion irradiation had a minor effect on τ_{e-ph} , increasing it by approximately 14% (from 11.2 ps to 12.8 ps). However, a 57% reduction in TBC, from $127 \text{ W/m}^2\text{K}^4$ to $54 \text{ W/m}^2\text{K}^4$, was observed, attributed to irradiation-induced disorder. TEM analysis confirmed the increased disorder at the NbN/SiO₂ interface and the formation of He-induced bubbles in the first SiO₂ layer. The fluence-dependent variation observed in our TBC measurements aligns with trends reported in the literature [45].

Table I. Contribution of thermal and electrical performance to the enhancement of IDE through irradiation (9×10^{16} ions cm^{-2}).

Performance category	Main parameter changes	Impact on IDE (sensitivity)	
Thermal	TBC $\downarrow 57\%$, τ_{hs-min} $\uparrow 41\%$, τ_{e-ph} $\uparrow 14\%$	<ul style="list-style-type: none"> Enhanced heat localization Increased quasiparticle lifetime 	I D
Electrical	N_0 $\downarrow 30\%$, D_c $\downarrow 6\%$, R_s $\uparrow 33\%$, Δ_0 $\downarrow 10\%$	<ul style="list-style-type: none"> Smaller N_0 and D_c improve thermalization Reduced Δ_0 and larger R_s \rightarrow hotspot growth 	E \uparrow

These thermal effects directly influence the τ_{hs-min} , which increased by 41% (from 17 ps to 24 ps) under irradiation. This change is substantial when compared to previous methods involving complex fabrication processes. For instance, NbN typically exhibits a low τ_{hs-min} value. In past studies [42], altering the substrate from SiO₂ to Si led to an increase in τ_{hs-min} from around 23 ps to 35 ps, marking a 95% increase from the initial value. Similarly, Xu et al. [38] achieved

a $\tau_{\text{hs-min}}$ increase from 24.6 ps to 50 ps (a 103% change) using a suspended SiO₂ membrane. Thus, He ion irradiation offers an alternative means of tuning the thermal properties of superconducting devices without altering the structures, making it an effective tool for modifying heat transport and studying the physical mechanism.

Table I summarizes the contributions of thermal and electrical factors to the enhancement of IDE through irradiation. Changes in electrical properties (Appendix Table III), including a 30% reduction in N_0 , a 33% increase in R_s , and a 10% reduction in energy gap (Δ_0 , at $T = 0$), also contribute to IDE enhancement. However, the relative contributions of thermal and electrical effects remain challenging to quantify, although thermal effects appear to play a significant role at high irradiation fluences [45].

Further studies could investigate the integration of multiple strategies or interface engineering to mitigate the effects of irradiation on thermal dissipation. For instance, combining irradiation with a suspended dielectric layer or mesa structure [39] could offer enhanced thermal isolation, allowing for more effective control of heat flow. These multi-strategy designs have the potential to extend the limits of spectral sensitivity in SNSPDs and high-temperature SNSPD developments. Also, simulations of heat flow transmission across cross-sectional interfaces, including heat transport dynamics and transmission times, will help identify the specific interface locations affecting TBC performance. Additionally, investigating the role of thermal fluctuations and other fluctuation effects in broadening the IDE transition could lead to a better understanding of the SNSPD's detection mechanisms.

6. Conclusion

In summary, our study demonstrates that He-ion irradiation is an effective post-fabrication technique for tailoring the thermal properties of NbN thin films, thereby optimizing SNSPD performance. We observe a significant reduction in thermal boundary conductance and an enhancement in electron-phonon interaction dynamics, which leads to prolonged hotspot relaxation times. TEM analysis reveals amorphization at the NbN/SiO₂ interface and the formation of He-induced bubbles in the first SiO₂ layer. These effects improve IDE by modifying phonon transport and interfacial heat dissipation.

With these modifications and the avalanche mechanism, we demonstrate enhanced IDE performance in SC-2SNAP detectors, featuring a clear saturation plateau at 2000 nm over a

wide temperature range from 2.7 K to 28 mK. As the temperature decreases, the irradiated NbN-based SNSPD exhibits a broader and steeper saturation plateau under 2000 nm illumination, indicating improved sensitivity at longer wavelengths. Thermal activation fitting suggests that thermal fluctuations at higher temperatures may contribute to the broadening of the IDE transition. Moreover, the exponential dependence of both the detection threshold current and transition width on temperature and photon energy—observed with apparent universality—offers informative insight into the underlying mechanisms of IDE broadening. Notably, the avalanche current ratio remains nearly constant across the 450–2000 nm range, indicating weak wavelength dependence and underscoring the potential of SC-2SNAP detectors for high-temperature and long-wavelength applications.

Our findings suggest that controlled ion irradiation can be a valuable tool for engineering SNSPDs with improved sensitivity and efficiency. This work also advances the understanding of the detection mechanisms of SNSPDs and defect engineering in superconducting materials, paving the way for tunable thermal dynamics in superconducting optoelectronics.

Acknowledgments: This work is supported by the Innovation Program for Quantum Science and Technology (Grant No. 2023ZD0300100), the National Natural Science Foundation of China (Grant Nos. 62371443 and 61971409), and the Shanghai Sailing Program (Grant No. 22YF1456500). W.-J. Zhang is supported by an outstanding member of the Youth Innovation Promotion Association, CAS (Y2023071). The authors thank Ruo-Yan Ma, Xiao-Yu Liu, Bao Gao, and Min Zhou for their technical support.

Author contributions: W.-J.Z. conceived and designed the experiments, H.-Y.Y., Y.-Z.W., and W.-J.Z. fabricated the samples, conducted the experiments, and collected the data. H.-Q. Y. and W. -T. W. assisted with ultralow-temperature measurements. H.-Y.Y. and W.-J.Z. analyzed the data and prepared the manuscript. All authors discussed the results and reviewed the manuscript.

Competing interests: The authors declare no competing interests.

Data and materials availability: The data that support the findings of this study are available from the corresponding author upon reasonable request.

References

- [1] A. E. Lita, D. V. Reddy, V. B. Verma, R. P. Mirin, and S. W. Nam, Development of superconducting single-photon and photon-number resolving detectors for quantum applications, *J. Lightwave Technol.* **40**, 7578 (2022).
- [2] Y. Liu, W.-J. Zhang, C. Jiang, J.-P. Chen, C. Zhang, W.-X. Pan, D. Ma, H. Dong, J.-M. Xiong, C.-J. Zhang, H. Li, R.-C. Wang, J. Wu, T.-Y. Chen, L. You, X.-B. Wang, Q. Zhang, and J.-W. Pan, Experimental Twin-Field Quantum Key Distribution over 1000 km Fiber Distance, *Phys. Rev. Lett.* **130**, 210801 (2023).
- [3] X. Zhang, W. Zhang, H. Zhou, X. Zhang, L. You, H. Li, D. Fan, Y. Pan, H. Yu, L. Li, and Z. Wang, NbN Superconducting Nanowire Single-Photon Detector With 90.5% Saturated System Detection Efficiency and 14.7 ps System Jitter at 1550 nm Wavelength, *IEEE J. Sel. Top. Quant. Electron.* **28**, 3803708 (2022).
- [4] L. You, Superconducting nanowire single-photon detectors for quantum information, *Nanophotonics* **9**, 2673 (2020).
- [5] J. Wang, F. Sciarrino, A. Laing, and M. G. Thompson, Integrated photonic quantum technologies, *Nat. Photon.* **14**, 273 (2020).
- [6] F. Wang, F. Ren, Z. Ma, L. Qu, R. Gourgues, C. Xu, A. Baghdasaryan, J. Li, I. E. Zadeh, J. W. N. Los, A. Fognini, J. Qin-Dregely, and H. Dai, In vivo non-invasive confocal fluorescence imaging beyond 1,700 nm using superconducting nanowire single-photon detectors, *Nat. Nanotechnol.* **17**, 653 (2022).
- [7] J. Chiles, I. Charaev, R. Lasenby, M. Baryakhtar, J. Huang, A. Roshko, G. Burton, M. Colangelo, K. Van Tilburg, A. Arvanitaki, S. W. Nam, and K. K. Berggren, New Constraints on Dark Photon Dark Matter with Superconducting Nanowire Detectors in an Optical Haloscope, *Phys. Rev. Lett.* **128**, 231802 (2022).
- [8] G. G. Taylor, A. B. Walter, B. Korzh, B. Bumble, S. R. Patel, J. P. Allmaras, A. D. Beyer, R. O'Brien, M. D. Shaw, and E. E. Wollman, Low-noise single-photon counting superconducting nanowire detectors at infrared wavelengths up to 29 μm , *Optica* **10**, 1672 (2023).
- [9] Y. P. Korneeva, D. Y. Vodolazov, A. V. Semenov, I. N. Florya, N. Simonov, E. Baeva, A. A. Korneev, G. N. Goltsman, and T. M. Klapwijk, Optical Single-Photon Detection in Micrometer-Scale NbN Bridges, *Phys. Rev. Appl.* **9**, 064037 (2018).
- [10] G.-Z. Xu, W.-J. Zhang, L.-X. You, J.-M. Xiong, X.-Q. Sun, H. Huang, X. Ou, Y.-M. Pan, C.-L. Lv, H. Li, Z. Wang, and X.-M. Xie, Superconducting microstrip single-photon detector with system detection efficiency over 90% at 1550 nm, *Photon. Res.* **9**, 958 (2021).
- [11] Y.-Z. Wang, W.-J. Zhang, X.-Y. Zhang, G.-Z. Xu, J.-M. Xiong, Z.-G. Chen, Y.-Y. Hong, X.-Y. Liu, P.-S. Yuan, L. Wu, Z. Wang, and L.-X. You, Free-space coupled, large-active-area superconducting microstrip single-photon detector for photon-counting time-of-flight imaging, *Appl. Opt.* **63**, 3130 (2024).
- [12] R. Ma, Z. Guo, D. Chen, X. Dai, Y. Xiao, C. Zhang, J. Xiong, J. Huang, X. Zhang, X. Liu, L. Rong, H. Li, X. Zhang, and L. You, Drone-based superconducting nanowire single-photon detection system with a detection efficiency of more than 90%, *Advanced Photonics Nexus* **4**, 026003 (2025).
- [13] I. Charaev, D. A. Bandurin, A. T. Bollinger, I. Y. Phinney, I. Drozdov, M. Colangelo, B. A. Butters, T. Taniguchi, K. Watanabe, X. He, O. Medeiros, I. Božović, P. Jarillo-Herrero, and K. K. Berggren, Single-photon detection using high-temperature superconductors, *Nat. Nanotechnol.* **18**, 343 (2023).
- [14] I. Charaev, E. K. Batson, S. Cherednichenko, K. Reidy, V. Drakinskiy, Y. Yu, S. Lara-Avila, J. D. Thomsen, M. Colangelo, F. Incalza, K. Ilin, A. Schilling, and K. K. Berggren, Single-photon detection using large-scale high-temperature MgB_2 sensors at 20 K, *Nat. Commun.* **15**, 3973 (2024).
- [15] B. G. Oripov, D. S. Rampini, J. Allmaras, M. D. Shaw, S. W. Nam, B. Korzh, and A. N. McCaughan, A superconducting nanowire single-photon camera with 400,000 pixels, *Nature* **622**, 730 (2023).
- [16] W. J. Zhang, J. Huang, C. J. Zhang, L. X. You, C. L. Lv, L. Zhang, H. Li, Z. Wang, and X. M. Xie, A 16-Pixel Interleaved Superconducting Nanowire Single-Photon Detector Array With A Maximum Count Rate Exceeding 1.5 GHz, *IEEE Trans. Appl. Supercond.* **29**, 2200204 (2019).
- [17] D. Y. Vodolazov, Single-Photon Detection by a Dirty Current-Carrying Superconducting Strip Based on the Kinetic-Equation

Approach, *Phys. Rev. Appl.* **7**, 034014 (2017).

- [18] A. Semenov, A. Engel, H. W. Hubers, K. Il'in, and M. Siegel, Spectral cut-off in the efficiency of the resistive state formation caused by absorption of a single-photon in current-carrying superconducting nano-strips, *Eur. Phys. J. B* **47**, 495 (2005).
- [19] F. Marsili, V. B. Verma, J. A. Stern, S. Harrington, A. E. Lita, T. Gerrits, I. Vayshenker, B. Baek, M. D. Shaw, R. P. Mirin, and S. W. Nam, Detecting single infrared photons with 93% system efficiency, *Nat. Photon.* **7**, 210 (2013).
- [20] W. J. Zhang, L. X. You, H. Li, J. Huang, C. L. Lv, L. Zhang, X. Y. Liu, J. J. Wu, Z. Wang, and X. M. Xie, NbN superconducting nanowire single photon detector with efficiency over 90% at 1550 nm wavelength operational at compact cryocooler temperature, *Sci. China Phys. Mech. Astron.* **60**, 120314 (2017).
- [21] A. G. Kozorezov, C. Lambert, F. Marsili, M. J. Stevens, V. B. Verma, J. P. Allmaras, M. D. Shaw, R. P. Mirin, and S. W. Nam, Fano fluctuations in superconducting-nanowire single-photon detectors, *Phys. Rev. B* **96**, 054507 (2017).
- [22] M. Caloz, B. Korzh, N. Timoney, M. Weiss, S. Gariglio, R. J. Warburton, C. Schönenberger, J. Renema, H. Zbinden, and F. Bussi eres, Optically probing the detection mechanism in a molybdenum silicide superconducting nanowire single-photon detector, *Appl. Phys. Lett.* **110**, 083106 (2017).
- [23] X. Zhang, A. E. Lita, M. Sidorova, V. B. Verma, Q. Wang, S. W. Nam, A. Semenov, and A. Schilling, Superconducting fluctuations and characteristic time scales in amorphous WSi, *Phys. Rev. B* **97**, 174502 (2018).
- [24] H. Bartolf, A. Engel, A. Schilling, K. Il'in, M. Siegel, H. W. H ubers, and A. Semenov, Current-assisted thermally activated flux liberation in ultrathin nanopatterned NbN superconducting meander structures, *Phys. Rev. B* **81**, 024502 (2010).
- [25] V. B. Verma, B. Korzh, A. B. Walter, A. E. Lita, R. M. Briggs, M. Colangelo, Y. Zhai, E. E. Wollman, A. D. Beyer, J. P. Allmaras, H. Vora, D. Zhu, E. Schmidt, A. G. Kozorezov, K. K. Berggren, R. P. Mirin, S. W. Nam, and M. D. Shaw, Single-photon detection in the mid-infrared up to 10 μm wavelength using tungsten silicide superconducting nanowire detectors, *APL Photonics* **6**, 056101 (2021).
- [26] Y. Pan, H. Zhou, X. Zhang, H. Yu, L. Zhang, M. Si, H. Li, L. You, and Z. Wang, Mid-infrared Nb₄N₃-based superconducting nanowire single photon detectors for wavelengths up to 10 μm , *Opt. Express* **30**, 40044 (2022).
- [27] J. Zichi, J. Chang, S. Steinhauer, K. von Fieandt, J. W. N. Los, G. Visser, N. Kalhor, T. Lettner, A. W. Elshaari, I. E. Zadeh, and V. Zwiller, Optimizing the stoichiometry of ultrathin NbTiN films for high-performance superconducting nanowire single-photon detectors, *Opt. Express* **27**, 26579 (2019).
- [28] S. A. Cybart, E. Y. Cho, T. J. Wong, B. H. Wehlin, M. K. Ma, C. Huynh, and R. C. Dynes, Nano Josephson superconducting tunnel junctions in YBa₂Cu₃O_{7- δ} directly patterned with a focused helium ion beam, *Nat. Nanotechnol.* **10**, 598 (2015).
- [29] W.-J. Zhang, Q. Jia, L. You, X. Ou, H. Huang, L. Zhang, H. Li, Z. Wang, and X. Xie, Saturating Intrinsic Detection Efficiency of Superconducting Nanowire Single-Photon Detectors via Defect Engineering, *Phys. Rev. Appl.* **12**, 044040 (2019).
- [30] W.-J. Zhang, G.-Z. Xu, L.-X. You, C.-J. Zhang, H. Huang, X. Ou, X.-Q. Sun, J.-M. Xiong, H. Li, Z. Wang, and X.-M. Xie, Sixteen-channel fiber array-coupled superconducting single-photon detector array with average system detection efficiency over 60% at telecom wavelength, *Opt. Lett.* **46**, 1049 (2021).
- [31] S. Strohauser, F. Wietschorke, L. Zugliani, R. Flaschmann, C. Schmid, S. Grotowski, M. M uller, B. Jonas, M. Althammer, R. Gross, K. M uller, and J. J. Finley, Site-Selective Enhancement of Superconducting Nanowire Single-Photon Detectors via Local Helium Ion Irradiation, *Adv. Quantum Technol.* **2023**, 2300139 (2023).
- [32] K. Kohop a , A. Ronzani, R. N. Jabdaraghi, A. Bera, M. Ribeiro, D. Hazra, J. Senior, M. Prunnila, J. Govenius, J. S. Lehtinen, and A. Kemppinen, Effect of ion irradiation on superconducting thin films, *APL Materials* **12** (2024).
- [33] E. Batson, F. Incalza, M. Castellani, M. Colangelo, I. Charaev, A. Schilling, S. Cherednichenko, and K. K. Berggren, Effects of Helium Ion Exposure on the Single-Photon Sensitivity of MgB₂ and NbN Detectors, *IEEE Trans. Appl. Supercond.* **34**, 0600906 (2024).
- [34] E. M. Baeva, M. V. Sidorova, A. A. Korneev, K. V. Smirnov, A. V. Divochy, P. V. Morozov, P. I. Zolotov, Y. B. Vakhtomin, A. V. Semenov, T. M. Klapwijk, V. S. Khrapai, and G. N. Goltsman, Thermal Properties of NbN Single-Photon Detectors, *Phys. Rev. Appl.* **10**, 064063 (2018).

- [35] M. Sidorova, A. Semenov, H.-W. Hübers, K. Ilin, M. Siegel, I. Charaev, M. Moshkova, N. Kaurova, G. N. Goltsman, X. Zhang, and A. Schilling, Electron energy relaxation in disordered superconducting NbN films, *Phys. Rev. B* **102**, 054501 (2020).
- [36] E. M. Baeva, N. A. Titova, L. Veyrat, B. Sacépé, A. V. Semenov, G. N. Goltsman, A. I. Kardakova, and V. S. Khrapai, Thermal Relaxation in Metal Films Limited by Diffuson Lattice Excitations of Amorphous Substrates, *Phys. Rev. Appl.* **15**, 054014 (2021).
- [37] A. Dane, J. Allmaras, D. Zhu, M. Onen, M. Colangelo, R. Baghdadi, J.-L. Tambasco, Y. Morimoto, I. E. Forno, I. Charaev, Q. Zhao, M. Skvortsov, A. Kozorezov, and K. K. Berggren, Self-heating hotspots in superconducting nanowires cooled by phonon black-body radiation, *Nat. Commun.* **13**, 5429 (2022).
- [38] T. Xu, H. Bao, Z. Qin, X. Jia, G. Zhu, D. Pan, X. Tu, L. Zhang, Q. Zhao, L. Kang, J. Chen, and P. Wu, Enhancing SNSPDs detection efficiency via suspended SiO₂ membrane, *Appl. Phys. Lett.* **123**, 082602 (2023).
- [39] A. Stockhausen, K. Il'in, M. Siegel, U. Södervall, P. Jedrasik, A. Semenov, and H. W. Hübers, Adjustment of self-heating in long superconducting thin film NbN microbridges, *Supercond. Sci. Technol.* **25**, 035012 (2012).
- [40] A. D. Semenov, G. N. Gol'tsman, and R. Sobolewski, Hot-electron effect in superconductors and its applications for radiation sensors, *Supercond. Sci. Technol.* **15**, R1 (2002).
- [41] F. Marsili, M. J. Stevens, A. Kozorezov, V. B. Verma, C. Lambert, J. A. Stern, R. D. Horansky, S. Dyer, S. Duff, D. P. Pappas, A. E. Lita, M. D. Shaw, R. P. Mirin, and S. W. Nam, Hotspot relaxation dynamics in a current-carrying superconductor, *Phys. Rev. B* **93**, 094518 (2016).
- [42] L. Zhang, L. You, X. Yang, J. Wu, C. Lv, Q. Guo, W. Zhang, H. Li, W. Peng, Z. Wang, and X. Xie, Hotspot relaxation time of NbN superconducting nanowire single-photon detectors on various substrates, *Sci. Rep.* **8**, 1486 (2018).
- [43] A. D. Semenov, R. S. Nebosis, Y. P. Gousev, M. A. Heusinger, and K. F. Renk, Analysis of the nonequilibrium photoresponse of superconducting films to pulsed radiation by use of a two-temperature model, *Phys. Rev. B* **52**, 581 (1995).
- [44] M. Sidorova, A. D. Semenov, H. W. Hübers, S. Gyger, S. Steinhauer, X. Zhang, and A. Schilling, Magnetoconductance and photoresponse properties of disordered NbTiN films, *Phys. Rev. B* **104**, 184514 (2021).
- [45] Stefan Strohauer, Fabian Wietschorke, Markus Doblinger, Christian Schmid, Stefanie Grotowski, Lucio Zugliani, Bjorn Jonas, Kai Muller, and a. J. J. Finley, Origin of performance enhancement of superconducting nanowire single-photon detectors by He-ion irradiation, *arXiv*, 2501.14965v1 (2025).
- [46] F. Najafi, A. Dane, F. Bellei, Q. Zhao, K. Sunter, A. N. McCaughan, and K. K. Berggren, Fabrication Process Yielding Saturated Nanowire Single-Photon Detectors With 24-ps Jitter, *IEEE J. Sel. Top. Quant. Electron.* **21**, 3800507 (2015).
- [47] S. Miki, M. Yabuno, T. Yamashita, and H. Terai, Stable, high-performance operation of a fiber-coupled superconducting nanowire avalanche photon detector, *Opt. Express* **25**, 6796 (2017).
- [48] F. Marsili, F. Najafi, E. Dauler, F. Bellei, X. L. Hu, M. Csete, R. J. Molnar, and K. K. Berggren, Single-photon detectors based on ultranarrow superconducting nanowires, *Nano Lett.* **11**, 2048 (2011).
- [49] C. J. Zhang, W. J. Zhang, J. Huang, L. X. You, H. Li, C. L. Lv, T. Sugihara, M. Watanabe, H. Zhou, Z. Wang, and X. M. Xie, NbN superconducting nanowire single-photon detector with an active area of 300 μm -in-diameter, *AIP Adv.* **9**, 075214 (2019).
- [50] S. R. Patel, M. Colangelo, A. D. Beyer, G. G. Taylor, J. P. Allmaras, B. Bumble, E. E. Wollman, M. D. Shaw, K. K. Berggren, and B. Korzh, Improvements of readout signal integrity in mid-infrared superconducting nanowire single-photon detectors, *Appl. Phys. Lett.* **124**, 162604 (2024).
- [51] F. Marsili, F. Bellei, F. Najafi, A. E. Dane, E. A. Dauler, R. J. Molnar, and K. K. Berggren, Efficient single photon detection from 500 nm to 5 μm wavelength, *Nano Lett.* **12**, 4799 (2012).